APPLIED PHYSICS

Tailoring emergent spin phenomena in Dirac material heterostructures

Dmitrii Khokhriakov[1], Aron W. Cummings[2], Kenan Song[2,3], Marc Vila[2,3], Bogdan Karpiak[1], André Dankert[1], Stephan Roche[2,4]*, Saroj P. Dash[1,5]*

Dirac materials such as graphene and topological insulators (TIs) are known to have unique electronic and spintronic properties. We combine graphene with TIs in van der Waals heterostructures to demonstrate the emergence of a strong proximity-induced spin-orbit coupling in graphene. By performing spin transport and precession measurements supported by ab initio simulations, we discover a strong tunability and suppression of the spin signal and spin lifetime due to the hybridization of graphene and TI electronic bands. The enhanced spin-orbit coupling strength is estimated to be nearly an order of magnitude higher than in pristine graphene. These findings in graphene-TI heterostructures could open interesting opportunities for exploring exotic physical phenomena and new device functionalities governed by topological proximity effects.

INTRODUCTION

Heterostructures of materials with complementary electronic and topological properties have served as a foundation for designing novel physical states in condensed matter physics. Recently, Dirac materials such as graphene (Gr) and topological insulators (TIs) have attracted considerable attention in the context of their uniquely similar linear energy band spectra, which are well described as massless two-dimensional (2D) chiral Dirac fermions (*1*). Although these materials have similar surface energy spectra, the key difference between them lies in their spin-orbit coupling (SOC) strength. Graphene is a material with large carrier mobility and very low intrinsic SOC, giving rise to long spin coherence lengths at room temperature (*2*–*5*). In contrast, the topological Dirac surface states emerging in bulk-insulating TIs are generated by strong SOC, which gives rise to their helical spin-momentum locking feature (*6*). Beyond the scientific relevance of these Dirac materials, assembling them in van der Waals heterostructures (vdWhs) is promising to engineer new electronic and spintronic properties, which have no equivalent in the individual materials.

Heterostructures of Gr and TIs have been proposed for realizing an emergent topological quantum spin Hall phase. It has been predicted that in Gr-TI heterostructures, the electronic spectrum of Gr becomes gapped (~2 to 20 meV), develops heavy Dirac fermions, and acquires a unique spin texture (*7*–*12*). Experimentally, photoemission experiments on Gr-TI heterostructures suggest the coexistence of topological surface states and Dirac π bands of Gr (*13*, *14*). Recently, Gr-TI heterostructures have been used for spin injection into Gr (*15*), with reports of anomalous quantum transport behavior (*16*) and quantum tunneling processes (*17*–*19*). Finally, the prediction of a giant Edelstein effect could open avenues for the use of current-induced spin-orbit torques in nonvolatile memory technologies (*20*). Although these studies indicate that Gr-TI heterostructures can emerge as a new paradigm for spintronic applications, the proximity-induced SOC has not yet been experimentally investigated, and the nature of the spin relaxation remains unknown.

Here, we report the emergence of a strong SOC in Dirac material heterostructures of Gr and TIs by combining spin-polarized electron transport experiments and ab initio simulations. We take advantage of the excellent spin transport properties of Gr to unveil and analyze the nature of the proximity-induced spin physics in these 2D vdWhs. By integrating Gr with two TI materials having different doping levels, Bi_2Se_3 (BS) and $Bi_{1.5}Sb_{0.5}Te_{1.7}Se_{1.3}$ (BSTS), we find strong proximity-induced SOC that indicates substantial hybridization of the electronic bands of Gr and TIs. The modulation of the spin signal magnitude and

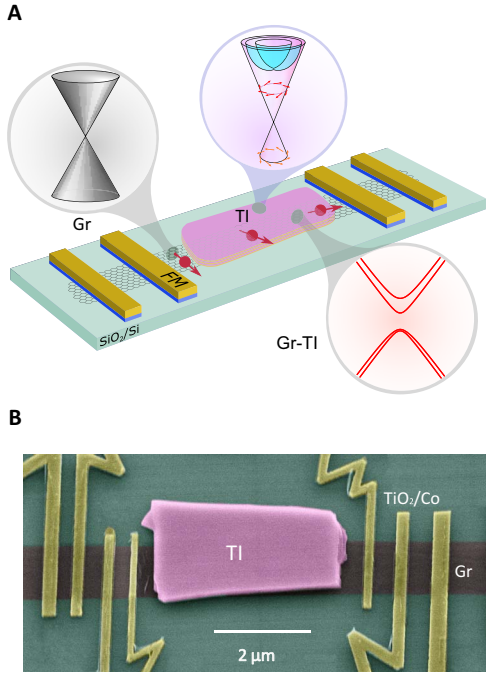

Fig. 1. Gr-TI heterostructure. (**A**) Schematic representation of a device consisting of a Gr-TI heterostructure channel and ferromagnetic (FM) tunnel contacts for spin injection and detection in a nonlocal transport geometry. The insets show the band structures of Gr and TI, as well as the splitting in Gr bands expected in a heterostructure region. (**B**) SEM micrograph of the fabricated device showing the Gr-TI heterostructure channel with FM tunnel contacts of TiO_2 (1 nm)/Co (60 nm) on Gr. Scale bar, 2 μm.

[1]Department of Microtechnology and Nanoscience, Chalmers University of Technology, SE-41296 Göteborg, Sweden. [2]Catalan Institute of Nanoscience and Nanotechnology (ICN2), Consejo Superior de Investigaciones Científicas (CSIC) and Barcelona Institute of Science and Technology (BIST), Campus Universitat Autònoma de Barcelona (UAB), Bellaterra, 08193 Barcelona, Spain. [3]Universitat Autònoma de Barcelona, Campus UAB, Bellaterra, 08193 Barcelona, Spain. [4]ICREA, Institució Catalana de Recerca i Estudis Avançats, 08070 Barcelona, Spain. [5]Graphene Center, Chalmers University of Technology, SE-41296 Göteborg, Sweden.
*Corresponding author. Email: stephan.roche@icn2.cat (S.R.); saroj.dash@chalmers.se (S.P.D.)

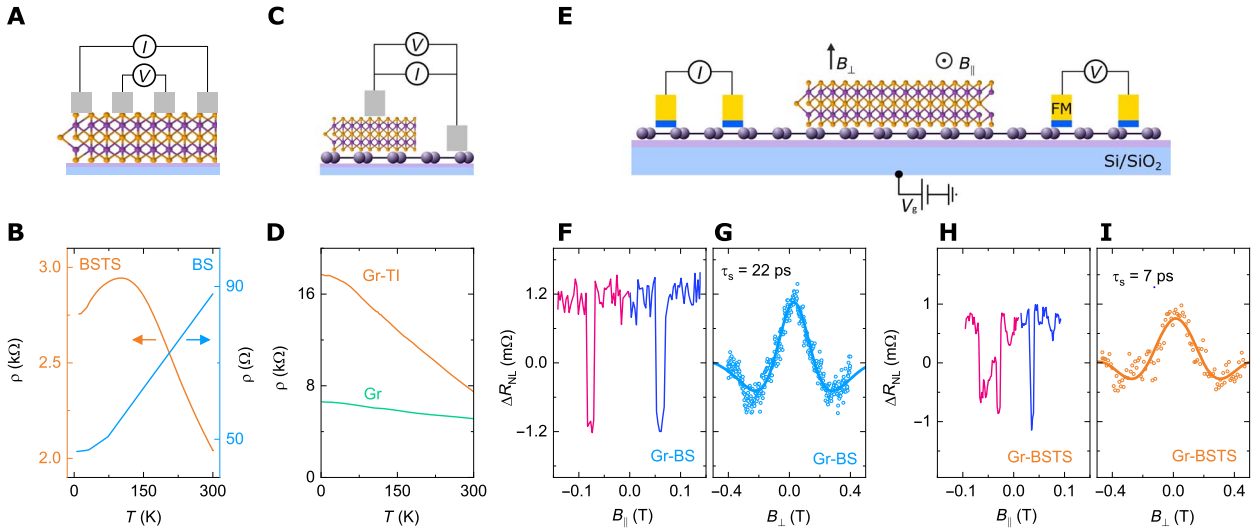

Fig. 2. Electrical and spin transport in Gr-TI heterostructures. (**A**) Schematic of four-terminal local geometry used for measurement of electrical resistance and magnetotransport in TI materials. (**B**) Temperature dependence of the channel resistance for BS and BSTS. (**C**) Schematic of measurement configuration of vertical Gr-TI heterostructure channels. (**D**) Temperature dependence of two-terminal resistivity in a Gr-BSTS heterostructure and a Gr channel. (**E**) Schematic of nonlocal measurement configuration used for spin-valve and Hanle experiments. (**F** and **G**) Spin-valve and Hanle measurements in a Gr-BS heterostructure. Hanle data are fitted using Eq. 1 to extract spin precession parameters. (**H** and **I**) Spin-valve and Hanle measurements in a Gr-BSTS heterostructure.

spin lifetime with gate voltage provide a fundamental understanding of the strength and nature of the proximity-induced spin interaction in Gr-TI heterostructures and suggest possible spintronic device functionalities.

RESULTS AND DISCUSSION

Fabrication and characterization of Gr-TI heterostructures

Figure 1 (A and B) shows a schematic and a scanning electron microscope (SEM) picture, respectively, of the spintronic device consisting of a Gr-TI heterostructure (see Methods for details of the nanofabrication process). We have chosen hybrid structures of chemical vapor–deposited (CVD) Gr with two different TI compounds, BS and BSTS, because of their different doping levels. The BS is heavily doped with the Fermi level (E_F) lying inside the bulk conduction band, whereas BSTS is low-doped with E_F in the bulk bandgap. These properties are reflected in the temperature dependence of the TI channel resistance measurements (Fig. 2, A and B). While BS shows metallic bulk-band conduction across all temperatures, the low doping of BSTS leads to semiconducting behavior at high temperatures and a dominating metallic Dirac surface state transport below 100 K (Fig. 2B) (*21*). The gate dependence studies of BS and BSTS confirm that both materials are n-type (fig. S1). While BS shows a very weak gate dependence, the resistance modulation of BSTS is more substantial (more details in section S1). Magnetotransport measurements show weak anti-localization (WAL) behavior of BS and BSTS, indicating strong SOC in the topological materials (fig. S2). To evaluate the degree of coupling between TIs and Gr, we performed electrical transport measurements in the vertical heterostructure geometry (Fig. 2C). The heterostructure junctions show a stronger temperature dependence compared to Gr (Fig. 2D). Further electrical characterization of heterostructure interfaces reveals the presence of a tunneling behavior with a zero-bias resistance ranging in different devices between 15 and 30 kΩ. Figures S3 and S4 show the current-voltage characteristics and Raman spectra of Gr-TI heterostructures, indicating good material and interface quality.

Spin transport measurements in Gr-TI heterostructures

To determine the nature of spin transport and relaxation in the Gr-TI heterostructures, we performed spin-valve and Hanle spin precession measurements in the nonlocal (NL) configuration (Fig. 2E). FM tunnel contacts of Co/TiO_2 are used for injection and detection of spin-polarized current in the heterostructure channel. For spin-valve measurements, we record the nonlocal resistance ($\Delta R_{NL} = \Delta V_{NL}/I$) while sweeping the in-plane magnetic field ($B_\parallel$) along the easy axis of the FM contacts to achieve parallel and antiparallel magnetization configurations. The Hanle spin precession measurements were performed with an applied out-of-plane magnetic field ($B_\perp$). We observe clear spin-valve and Hanle signals in both the Gr-BS and Gr-BSTS heterostructure devices, as shown in Fig. 2 (F to I). Hanle signals are fitted with Eq. 1

$$\Delta R_{NL} \propto \int_0^\infty \frac{1}{\sqrt{4\pi D_s t}} e^{-\frac{L^2}{4D_s t}} \cos(\omega_L t) \exp\left(\frac{-t}{\tau_s}\right) dt \qquad (1)$$

where a small $B_\perp$ field induces spin precession with the Larmor frequency $\omega_L = \frac{g\mu_B}{\hbar} B_\perp$, resulting in dephasing of the spin polarization while keeping the magnetization of FM contacts in-plane.

We observe a nonlocal spin signal $\Delta R_{NL} \approx 0.3$ to 2.2 mΩ in both Gr-BS and Gr-BSTS heterostructures. From Hanle data (Fig. 2, G and I), we extract spin lifetime $\tau_s = 22$ ps for Gr-BS and 7 ps for Gr-BSTS devices with spin diffusion constants $D_s = 0.01$ and 0.007 $m^2\ s^{-1}$ and spin diffusion lengths $\lambda_s = \sqrt{D_s \tau_s} = 0.5$ and 0.2 μm, respectively. These devices have channel lengths $L = 2.5$ μm for Gr-BS and 3.8 μm for Gr-BSTS. The obtained values of spin parameters are strongly reduced compared to pristine Gr devices with similar L, which exhibit $\Delta R_{NL} \approx 2$ to 4 Ω and $\tau_s = 400$ to 800 ps, as was systematically studied previously in similar Gr samples by our group (*5*). This reduction in spin parameters by two orders of magnitude in our Gr-TI heterostructures can be attributed to strong proximity-induced SOC in the Gr layer, as was predicted by theoretical calculations (*7*, *8*, *12*, *22*) and observed experimentally in devices composed of Gr and 2D semiconductors (*23*–*27*).

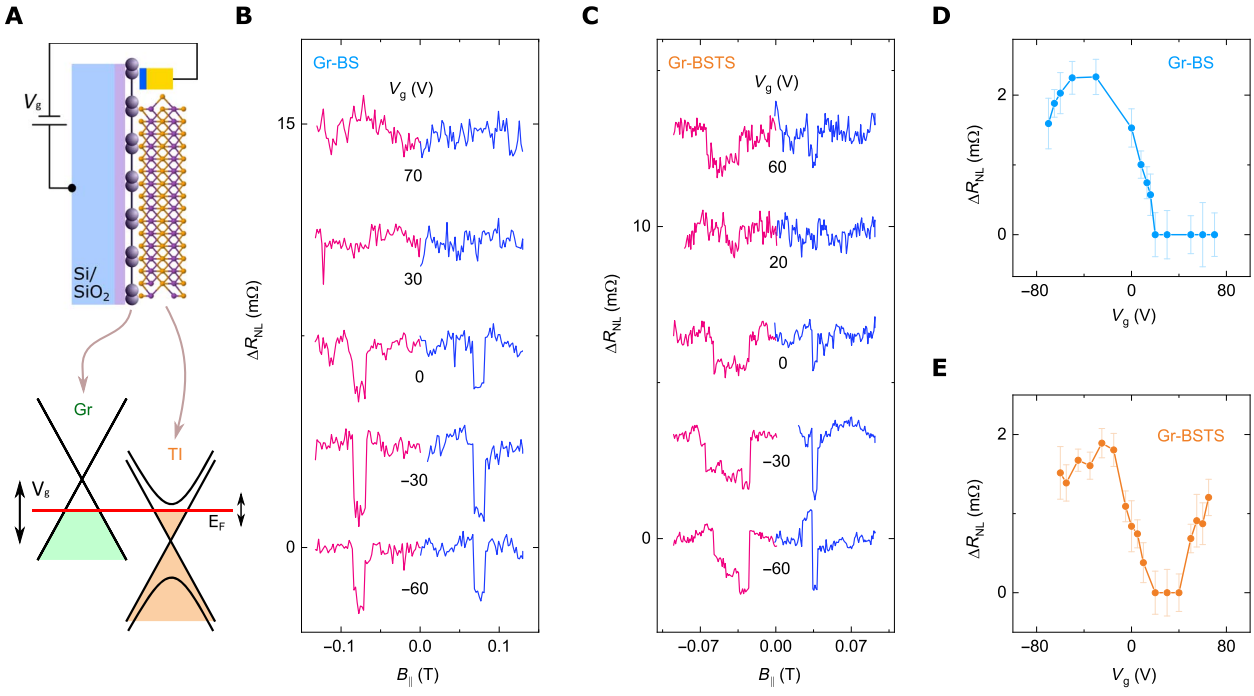

Fig. 3. Gate dependence of spin-valve signals in Gr-TI heterostructures. (**A**) Schematic of the Gr-TI heterostructure with an applied gate voltage (V_g) over the SiO_2 layer, using n^{++} Si as a gate electrode. This mainly affects the Fermi level position in Gr, with smaller variation in the TIs due to their higher doping and screening of gate voltage by Gr. (**B**) Spin-valve signals ΔR_{NL} in Gr-BS heterostructure measured at different gate voltages V_g. (**C**) Spin-valve signals in Gr-BSTS heterostructures measured at different gate voltages. (**D** and **E**) Gate dependence of spin-valve signal amplitude ΔR_{NL} in Gr-BS and Gr-BSTS heterostructures, respectively.

Gate dependence of spin signal in Gr-TI heterostructures

To further investigate the spin interaction strength in the Gr-TI heterostructures, we studied the effect of perpendicular electric field on the spin signals by applying back gate voltage (V_g; Fig. 3A). Tuning the Fermi level alignment and carrier density by gate voltage in both the Gr-BS (Fig. 3, B and D) and Gr-BSTS (Fig. 3, C and E) heterostructures results in a strong modulation of ΔR_{NL}, with the spin signal disappearing at positive V_g and subsequently reappearing at higher V_g in the case of Gr-BSTS. The measurements were performed at temperature $T = 70$ K, and the results were reproduced in other devices up to room temperature (figs. S5 and S6). To further clarify the dependence of the spin relaxation on V_g, we performed gate-dependent Hanle spin precession measurements (Fig. 4). Similar to the outcomes seen for the spin-valve signal, we observe a strong modulation of the Hanle amplitude ΔR_{NL} and spin lifetime τ_s as the Fermi level E_F approaches the Dirac point of Gr [Fig. 4, A to D (for Gr-BS devices) and E to H (for Gr-BSTS devices)]. By applying V_g, we mainly modulate the Fermi level position in Gr, while in BS, the E_F remains in the conduction band (E_c) because of high n-type doping, and in BSTS, we expect a small increase of E_F toward the conduction band, since E_F resides in the Dirac surface states ~22 meV below the conduction band edge, as calculated using a measured carrier density of $n_{2D} = 5 \times 10^{12}$ cm^{-2} (*21*). For a discussion of the difference in Gr Fermi level position in heterostructures and the influence of TIs on Gr doping, see fig. S7 and section S2.

Although there are electrostatic differences between the Gr-BS and Gr-BSTS heterostructures, the spin transport measurements reveal a common feature—the spin signal is strongly suppressed when the Fermi level approaches the Gr Dirac point (V_D). We can consider several mechanisms that can be responsible for this behavior. The first is a spin absorption effect, where transport is shunted from Gr into the TI layer. Away from the Dirac point, the Gr resistance is small such that most transport happens in the Gr layer, and the spin signal is thus dominated by the spin relaxation properties of the Gr in proximity with TIs. Near the Dirac point, the Gr resistance is increased, which could divert transport into the adjacent TI layer. Because of its high SOC, spin relaxation is expected to be very fast in the TI conduction band, which then reduces the detected spin signal. However, the Gr resistivity in our devices at all gate voltages and temperatures remains below 8 kΩ (see Figs. 2D and 4, B and F), while zero-bias Gr-TI junction resistance of ~15 to 30 kΩ (fig. S3C) can limit spin absorption effects by strongly restricting the spin diffusion current to the Gr layer. This is in contrast to recent measurements of Gr in heterostructures with MoS_2 and WS_2, where the observed spin signal modulation is attributed to the presence of a gate-tunable Schottky barrier and SOC at the interface (*23*–*25*), while in our heterostructures, the tunneling interface resistance between TIs and Gr is weakly dependent on gate (fig. S3, A to C). Another mechanism that could cause a modulation of spin parameters is the conductivity mismatch between the Gr and the FM tunnel contacts, driven by a tuning of the Gr carrier density and resistivity with gate voltage (*5*, *28*). Further theoretical investigations propose an additional mechanism that can influence the spin relaxation in these heterostructures, namely, the novel spin texture induced in Gr due to the hybridization of Gr and TI bands.

Calculation of SOC in Gr-TI heterostructures

To better understand the proximity effect of TIs on the spin properties of Gr, we performed ab initio simulations of Gr in contact with a six–quintuple layer (QL) slab of BS (see Methods for details). Figure 5A shows the band structure of the Gr-BS heterostructure, with blue, green, and red symbols indicating states that reside in the TI surface in contact

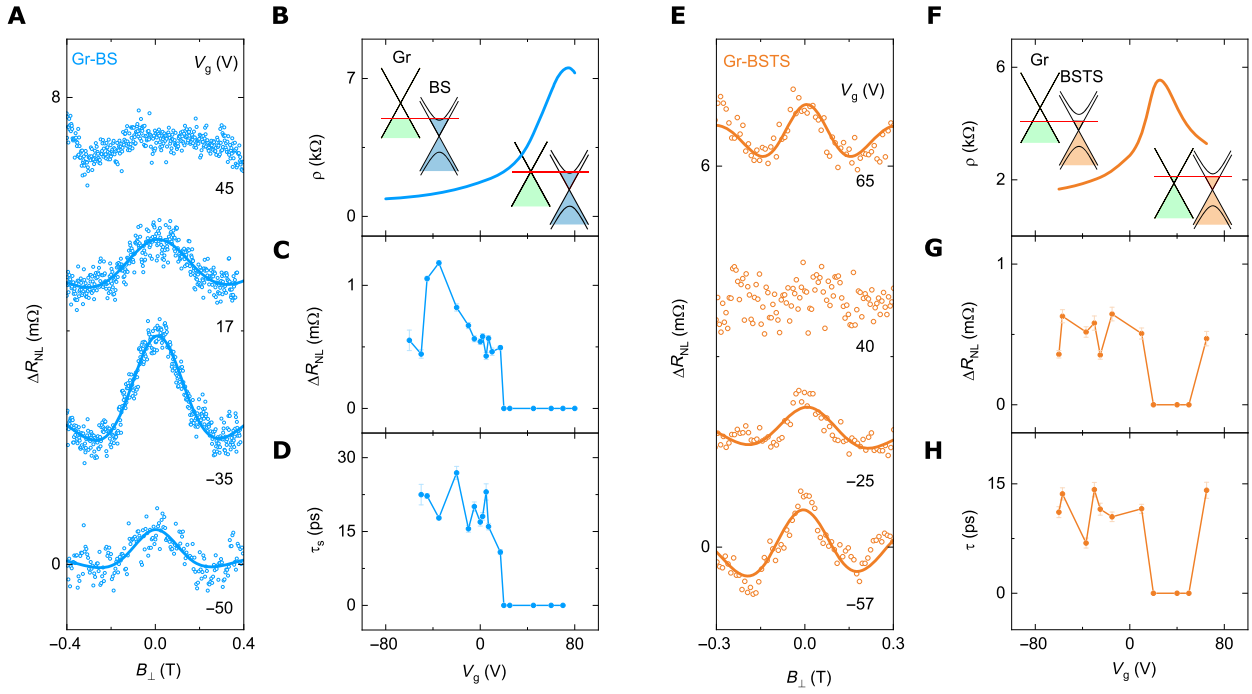

Fig. 4. Gate dependence of the Hanle signal in Gr-TI heterostructures. (**A**) Hanle spin signal ΔR_{NL}, measured in a Gr-BS device at different back gate voltages (V_g). (**B** to **D**) Gate voltage dependence of the channel sheet resistivity ρ, Hanle signal amplitude ΔR_{NL}, and spin lifetime τ_s measured in the Gr-BS device. Inset shows the Gr-BS band structures at two representative gate voltages. (**E**) Nonlocal Hanle spin precession measurements for a Gr-BSTS device at different V_g. (**F** to **H**) Gate voltage dependence of ρ, ΔR_{NL}, and τ_s for the Gr-BSTS device. Inset shows the Gr-BSTS band structures at two representative gate voltages.

with the Gr layer, the opposite TI surface, and the Gr layer, respectively. Purely black lines thus represent states in the bulk of the TI. The Gr is considered to be strongly p-doped with the Dirac point far above the Fermi level (dashed line), while the BS is n-doped with E_F in the bulk conduction band of the TI, in accordance to what is seen experimentally. The inset of Fig. 5A shows a zoom-in of the bands near the Gr Dirac point, indicating the presence of a spin splitting of 1.9 (1.2) meV in the conduction (valence) band away from the Dirac point, and a bandgap of 3.4 meV induced in the Gr layer by the TI. The symbols show the ab initio results, and the lines are a fit using a tight-binding model that captures both the band structure and spin texture induced in the Gr layer by the TI (*12*). The dominating spin-orbit terms in this model include an intrinsic SOC, also known as Kane-Mele SOC (*29*), with a strength λ_I = 0.83 meV, and a Rashba SOC arising from strong in-plane fields with a strength λ_R^ρ = 0.8 meV. These terms determine the spin splitting of the bands, while the bandgap arises from a combination of λ_I, λ_R^ρ, and a Kekulé distortion of the Gr lattice (*12*, *30*).

The spin texture of the Gr bands is shown in the inset of Fig. 5B, for energy contours between 14 and 155 meV away from the Gr Dirac point, with the color of the arrows denoting the out-of-plane component of the spin. Near the Dirac point, the spins are polarized primarily out of the Gr plane, while away from the Dirac point, the spins become primarily in-plane with a helical texture dictated by Rashba SOC. The main panel of Fig. 5B summarizes the Gr spin texture over a much larger energy range by showing the average in-plane spin polarization of the Gr bands at each energy (see Methods for details of this calculation). Except for near the Dirac point, the Gr bands are polarized primarily in the Gr plane with a helical spin texture, $\langle S_x^2\rangle = \langle S_y^2\rangle \approx 0.5$ and $\langle S_z^2\rangle \approx 0$, including the region where the Gr hybridizes with the TI bulk bands, −0.1 eV < $E - E_F$ < 0.2 eV.

In Fig. 5C, we plot the expected spin lifetime, derived from this particular band structure and by assuming the coexistence of the two usual mechanisms of SOC-induced spin relaxation in Gr, namely, the Elliott-Yafet (EY) and D'yakonov-Perel' (DP) mechanisms. The DP mechanism yields an inverse proportionality between τ_s and the momentum relaxation time τ_p, $\tau_{s,DP}^{-1} = \left(\overline{S^2} - \overline{S_x^2}\right)\left(\frac{2\Delta_{DP}}{\hbar}\right)^2\tau_p$, where $2\Delta_{DP}$ is the SOC-induced spin splitting of the band, $\overline{S^2}$ is the total spin polarization averaged over the Fermi surface, and $\overline{S_x^2}$ is the x component of the spin polarization averaged over the Fermi surface (*31*, *32*). In the case of a purely in-plane spin texture induced by Rashba SOC, this spin polarization prefactor is equal to $^1/_2$, giving $\tau_{s,DP}^{-1} = 2\left(\frac{\Delta_{DP}}{\hbar}\right)^2\tau_p$. The EY mechanism leads to direct scaling between τ_s and τ_p, $\tau_{s,EY} = \left(\frac{E_F - E_D}{\Delta_{EY}}\right)^2\tau_p$, where $E_F - E_D$ is the Fermi energy relative to the Gr Dirac point and Δ_{EY} is the EY SOC (*33*, *34*), typically arising from intrinsic SOC in the case of in-plane spin relaxation (*35*). The total spin relaxation time is $\tau_s = \left(\tau_{s,EY}^{-1} + \tau_{s,DP}^{-1}\right)^{-1}$. This quantity is plotted in Fig. 5C, assuming that $\Delta_{EY} = \lambda_I$ = 0.83 meV, $\Delta_{DP} \approx$ 0.6 meV is given by the valence band splitting extracted from the ab initio simulations, $(\overline{S^2} - \overline{S_x^2})$ is calculated as in Fig. 5B, and the values of E_F and τ_p are taken from the experimental measurements. This analysis predicts spin lifetimes on the order of a few tens of picoseconds with a strong decay near the Gr Dirac point, similar to what is seen experimentally. This decay near the Dirac point arises from a dominating EY mechanism at low electron densities.

We also consider the impact of spin absorption in the TI layer, which can affect the measured spin lifetime. Using a recently proposed model (*36*), we find that the spin relaxation arising from spin absorption is in

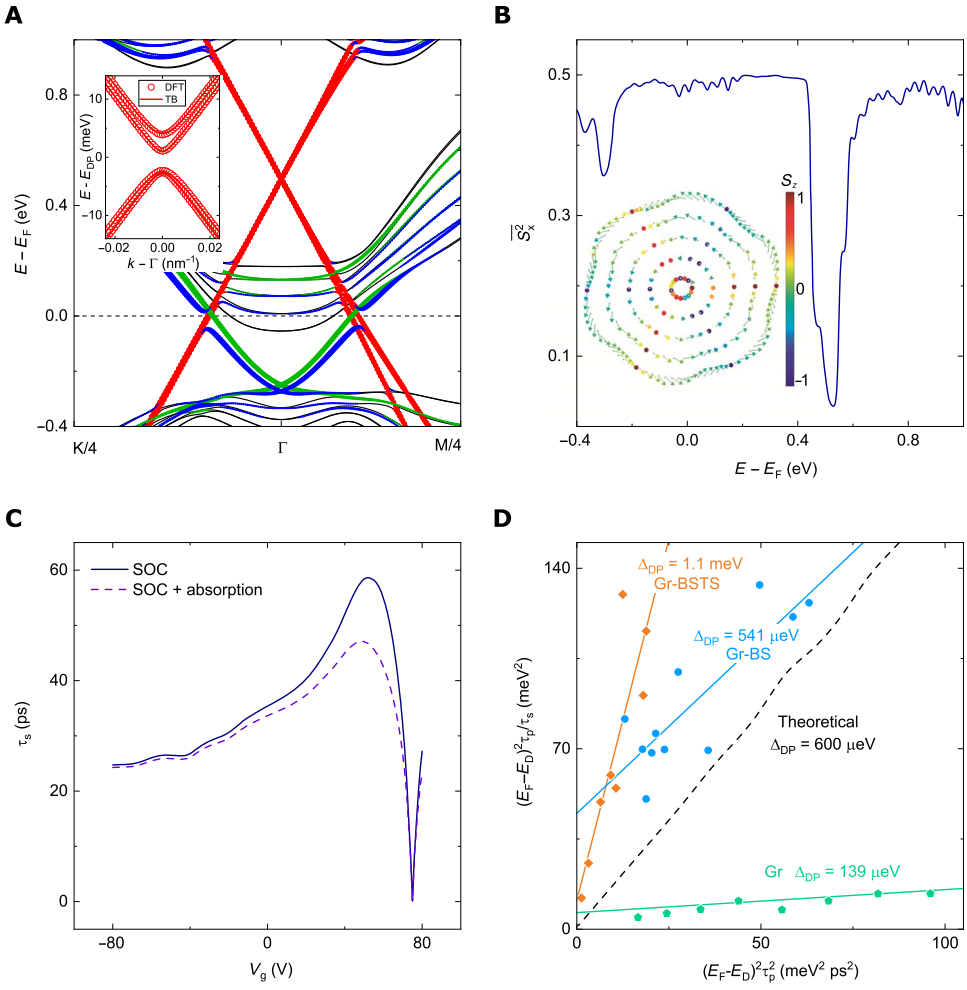

Fig. 5. Calculation of SOC strength and spin relaxation in Gr-TI heterostructures. (**A**) Calculated band structure of the Gr-BS hybrid structure, showing the BS surface state in proximity to Gr in blue, the opposite BS surface state in green, and Gr states in red. Inset: Zoom-in of the Gr bands around the Gr Dirac point, showing a bandgap and spin splitting on the order of millielectron volts. Open circles are ab initio results, while solid lines are the fit to a tight-binding model. (**B**) Calculated spin texture induced in Gr in proximity with BS. In the inset, the inner (outer) circle corresponds to an energy contour 14 (155) meV away from the Dirac point. The color scale indicates out-of-plane spin polarization, showing primarily out-of-plane (in-plane) spin polarization near (far from) the Gr Dirac point. The main panel shows the average in-plane spin polarization in Gr as a function of energy (gate voltage). Away from the Gr Dirac point, the spin polarization remains primarily in-plane. (**C**) Estimated spin lifetime in Gr arising from the ab initio band structure and spin texture, assuming spin relaxation dominated by the EY and DP mechanisms (solid line). The dashed line shows the predicted spin lifetime when including absorption of spins into the BS layer. (**D**) Estimation of SOC strength in Gr-SiO_2 (green), Gr-BS (blue), and Gr-BSTS (orange) devices extracted from experimental data in Fig. 4, using Eq. 2. The black dashed line shows the expected scaling based on the ab initio simulations.

the range of $\tau_{s,abs} = 150$ to 1200 ps (see section S3). The total spin lifetime including spin absorption effects, $\tau_s = (\tau_{s,EY}^{-1} + \tau_{s,DP}^{-1} + \tau_{s,abs}^{-1})^{-1}$, is shown as the dashed line in Fig. 5C. Here, we see that spin absorption can have a small impact close to the Dirac point, but overall, the spin relaxation is dominated by SOC proximity effects.

We note that our predicted spin lifetimes remain somewhat larger than the measured values, but this is not unreasonable considering that our analysis ignores other sources of spin relaxation, including dephasing by the contacts or by magnetic impurities (*37*–*39*). In addition, the range of gate voltages over which the spin signal is zero is much larger in the experiments than in our theoretical estimates. This could arise from enhanced hybridization when the Gr Dirac point aligns with the TI conduction bands, something that is neither captured in our ab initio simulations nor considered in the spin relaxation models. In addition, the spin signal is not necessarily zero in the experiments but rather falls below the noise level of the measurements.

To estimate the relative contributions of EY and DP spin relaxation in the measured spin lifetimes, the spin relaxation rate $\tau_s = \left(\tau_{s,EY}^{-1} + \tau_{s,DP}^{-1}\right)^{-1}$ can be rewritten as

$$(E_F - E_D)^2 \frac{\tau_p}{\tau_s} = \Delta_{EY}^2 + 2\left(\frac{\Delta_{DP}}{\hbar}\right)^2 (E_F - E_D)^2 \tau_p^2 \qquad (2)$$

We estimate τ_s from the Hanle analysis and τ_p from the gate dependence of the Gr-TI channel resistance using $\tau_p = \frac{2D_C}{v_F^2}$, where D_C is the charge diffusion coefficient and $v_F \approx 10^6$m/s is the Fermi velocity in Gr. Figure 5D shows the fits obtained with Eq. 2 for the Gr-BS and Gr-BSTS heterostructures, as well as for a reference pristine CVD Gr device on a SiO_2 substrate. The extracted values of the effective SOC for EY and DP mechanisms are $\Delta_{EY} = 6.7 \pm 0.8$ meV and $\Delta_{DP} = 541 \pm 56$ μeV for Gr-BS, $\Delta_{EY} = 3.3 \pm 2$ meV

and Δ_{DP} = 1.1 ± 0.1 meV for Gr-BSTS, and Δ_{EY} = 2.5 ± 0.4 meV and Δ_{DP} = 139 ± 6 μeV for pristine Gr. The values of Δ_{EY} are comparable with previous reports on Gr (*31*). We would like to note that because of variations in device parameters (channel length, contact resistance, Gr-TI overlap area, and relative lattice orientation), as well as variations in van der Waals interaction strength between Gr and TIs, the obtained values of the SOC strength cannot be directly compared between Gr-BS and Gr-BSTS heterostructures but rather used for qualitative comparison with the reference Gr device. In both Gr-TI heterostructures, we observe significantly higher values of Δ_{DP}, four to eight times higher than in pristine Gr, showing strong evidence of an increased proximity-induced SOC effect (*7*, *8*). For comparison, we also show the scaling obtained from the ab initio simulations; the value of Δ_{DP} is quite similar to those obtained experimentally, while the value of Δ_{EY} is somewhat smaller. However, we note that Δ_{EY} is also quite large in the reference Gr device, which can originate from non–SOC-driven spin relaxation mechanisms not considered in our analysis (*37*–*39*).

SUMMARY

The proximity-induced strong SOC in Dirac material heterostructures of Gr and TIs not only triggers the emergence of novel fundamental spin transport features but also can be useful for engineering spintronic functionalities inspired by topological phenomena. The advantage of these heterostructures is that, while Gr in proximity with TIs still supports good spin transport, concurrently, it acquires an induced strong SOC. This proximity-induced effect in Gr-TI systems could be further optimized by using TIs with a gate-tunable Fermi level and also by fully encapsulating Gr with TI materials from both sides (*40*). The SOC in Gr-TI heterostructures is also expected to be sensitive, and thus tunable, to adjustments of the twist angle between layers and by the application of strain and pressure in the heterostructures (*8*, *40*). These developments can lead to the emergence of a larger SOC-induced band splitting in Gr and possible realization of a robust well-quantized spin Hall effect at elevated temperatures in 2D material heterostructures (*6*, *41*–*43*). These achievements will open avenues for exploiting topological quantum effects, detecting exotic emergent particles, and pave the way for low-dissipation spin-based information processing technologies.

METHODS

Device fabrication

The vdWhs were prepared using CVD Gr from Graphenea on highly doped Si (with a thermally grown 285-nm-thick SiO_2 layer). The Gr was patterned by photolithography and oxygen plasma etching and cleaned afterward by Ar/H_2 annealing at 400°C for 90 min. The TI flakes (single crystals grown from a melt using a high vertical Bridgeman method, bought from Miracrys) were exfoliated by conventional scotch tape technique and dry-transferred on top of Gr. Next, appropriate 50- to 120-nm-thick BS or BSTS flakes located on Gr were identified by an optical microscope for device fabrication. The contacts were patterned on Gr (and TI flakes, in the case of vertical devices) by electron beam lithography. Finally, we used electron beam evaporation to deposit 1 nm of Ti, followed by in situ oxidation in a pure oxygen atmosphere for 2 hours to form a TiO_2 tunneling barrier layer. Without exposing the device to ambient atmosphere, in the same chamber, we deposited 60 nm of Co, after which the devices were finalized by liftoff in warm acetone at 65°C. In the final devices, the Co/TiO_2 contacts on Gr act as the source and drain for spin-polarized electrons, the Gr-TI heterostructure region serves as the channel, and the n^{++} Si/SiO_2 is used as a back gate.

The FM tunnel contact resistances (R_c), measured in three-terminal configuration, were around 1 kΩ. Raman spectra measured on BS, BSTS, Gr, and Gr-TI heterostructures show good quality of the materials and their heterostructures (fig. S4). The field-effect mobility of the Gr channel in proximity with TIs was 630 to 1500 $cm^2\ V^{-1}\ s^{-1}$. The observation of WAL in BS and BSTS and Shubnikov–de Haas (SdH) oscillations in BSTS shows the existence of a large spin-orbit interaction and 2D surface state conduction in the TI materials (*21*). The vertical transport properties of Gr-TI show tunneling behavior with an interface resistance of around 15 to 30 kΩ at zero-bias conditions (see fig. S3C).

Measurements

In the spin-valve measurements, changes in nonlocal voltage V_{NL} are observed when the magnetizations of the injector and detector FM contacts are changed to either parallel or antiparallel configuration by an in-plane external magnetic field. The measurements were performed in a flow cryostat and in a physical property measurement system at temperatures of 2 to 300 K and variable magnetic field. In the experiments, a bias current in the range of 75 to 500 μA was applied using a Keithley 6221 current source, and the nonlocal voltage was detected by a Keithley 2182A nanovoltmeter; the gate voltage was applied using a Keithley 2612 source meter.

Ab initio simulations

Ab initio calculations were carried out using density functional theory (*44*) implemented in the Vienna Ab initio Simulation Package (VASP) (*45*), with the wave functions expanded in a plane-wave basis with an energy cutoff of 600 eV, using the projector-augmented wave method (*46*). The Perdew-Burke-Ernzerhof (PBE) form of the generalized gradient approximation (*47*) was used to compute the exchange-correlation energy, and a 27 × 27 × 1 *k*-point mesh was used together with a convergence criterion of 10^{-6} eV. The SOC was included through noncollinear calculations, while the van der Waals force was accounted for on the basis of the Tkatchenko-Scheffler method (*48*), and all structures were fully relaxed until forces were smaller than 10^{-2} eV/Å. The unit cell consists of six carbon atoms centered over the Se atom in the top layer of BS, with a TI thickness of six QLs. In Fig. 5A, the surface states were identified by projecting the wave function at each *k*-point onto the atoms of the QL in contact with the Gr layer (blue symbols) or onto the atoms of the opposite QL (green symbols).

Average spin polarization calculation

The average spin polarization at a particular energy was calculated as the spin-polarized, carbon-projected density of states normalized by the carbon-projected density of states

$$\langle S_i^2 \rangle (E) = \sum_{n,\vec{k}} \left\{ \delta\left(E - E_{n,\vec{k}}\right) \left\langle \phi_{n,\vec{k}} | \sigma_i | \phi_{n,\vec{k}} \right\rangle^2 P^{C}_{n,\vec{k}} \right\} \Big/ \sum_{n,\vec{k}} \left\{ \delta\left(E - E_{n,\vec{k}}\right) P^{C}_{n,\vec{k}} \right\}$$

where $E_{n,\vec{k}}$ and $\phi_{n,\vec{k}}$ are the eigenenergy and eigenvector of band *n* at *k*-point $\vec{k}$, $P^{C}_{n,\vec{k}}$ is the projection of $\phi_{n,\vec{k}}$ onto the carbon atoms, σ_i are the spin Pauli matrices, and the δ functions are broadened as Fermi-Dirac distributions with a temperature of 75 K. The sums were carried out over a sample of ~8400 *k*-points distributed around the Γ point of the Brillouin zone.

SUPPLEMENTARY MATERIALS

Supplementary material for this article is available at http://advances.sciencemag.org/cgi/content/full/4/9/eaat9349/DC1

Section S1. Gate voltage dependence of TI resistance
Section S2. Doping of Gr by TIs
Section S3. Effect of spin absorption by TIs
Fig. S1. Gate dependence of TI resistance.
Fig. S2. Magnetotransport measurements in BS and BSTS.
Fig. S3. Electrical transport in Gr-TI heterostructures.
Fig. S4. Atomic force microscopy and Raman spectroscopy measurements of BS, BSTS, Gr, and Gr-TI heterostructures.
Fig. S5. Gate dependence of spin signals in another Gr-BS heterostructure device at room temperature.
Fig. S6. Gate dependence of spin signals in another Gr-BSTS heterostructure device at room temperature.
Fig. S7. Gr doping.
Fig. S8. Calculated spin lifetime due to spin absorption as a function of the Gr square resistance.
References (*49*–*52*)

REFERENCES AND NOTES

1. D. Pesin, A. H. MacDonald, Spintronics and pseudospintronics in graphene and topological insulators. *Nat. Mater.* **11**, 409–416 (2012).
2. S. Roche, J. Åkerman, B. Beschoten, J.-C. Charlier, M. Chshiev, S. P. Dash, B. Dlubak, J. Fabian, A. Fert, M. Guimarães, F. Guinea, I. Grigorieva, C. Schönenberger, P. Seneor, C. Stampfer, S. O. Valenzuela, X. Waintal, B. van Wees, Graphene spintronics: The European flagship perspective. *2D Mater.* **2**, 030202 (2015).
3. W. Han, R. K. Kawakami, M. Gmitra, J. Fabian, Graphene spintronics. *Nat. Nanotechnol.* **9**, 794–807 (2014).
4. N. Tombros, C. Jozsa, M. Popinciuc, H. T. Jonkman, B. J. van Wees, Electronic spin transport and spin precession in single graphene layers at room temperature. *Nature* **448**, 571–574 (2007).
5. M. V. Kamalakar, C. Groenveld, A. Dankert, S. P. Dash, Long distance spin communication in chemical vapour deposited graphene. *Nat. Commun.* **6**, 6766 (2015).
6. M. Z. Hasan, C. L. Kane, *Colloquium*: Topological insulators. *Rev. Mod. Phys.* **82**, 3045–3067 (2010).
7. K.-H. Jin, S.-H. Jhi, Proximity-induced giant spin-orbit interaction in epitaxial graphene on a topological insulator. *Phys. Rev. B* **87**, 075442 (2013).
8. J. Zhang, C. Triola, E. Rossi, Proximity effect in graphene–topological-insulator heterostructures. *Phys. Rev. Lett.* **112**, 096802 (2014).
9. W. Cao, R.-X. Zhang, P. Tang, G. Yang, J. Sofo, W. Duan, C.-X. Liu, Heavy Dirac fermions in a graphene/topological insulator hetero-junction. *2D Mater.* **3**, 034006 (2016).
10. C. De Beule, M. Zarenia, B. Partoens, Transmission in graphene–topological insulator heterostructures. *Phys. Rev. B* **95**, 115424 (2017).
11. H. Jin, J. Im, J.-H. Song, A. J. Freeman, Multiple Dirac fermions from a topological insulator and graphene superlattice. *Phys. Rev. B* **85**, 045307 (2012).
12. K. Song, D. Soriano, A. W. Cummings, R. Robles, P. Ordejón, S. Roche, Spin proximity effects in graphene/topological insulator heterostructures. *Nano Lett.* **18**, 2033–2039 (2018).
13. G. Bian, T.-F. Chung, C. Chen, C. Liu, T.-R. Chang, T. Wu, I. Belopolski, H. Zheng, S.-Y. Xu, D. S. Sanchez, N. Alidoust, J. Pierce, B. Quilliams, P. P. Barletta, S. Lorcy, J. Avila, G. Chang, H. Lin, H.-T. Jeng, M.-C. Asensio, Y. P. Chen, M. Zahid Hasa, Experimental observation of two massless Dirac-fermion gases in graphene-topological insulator heterostructure. *2D Mater.* **3**, 021009 (2016).
14. P. Lee, K.-H. Jin, S. J. Sung, J. G. Kim, M.-T. Ryu, H.-M. Park, S.-H. Jhi, N. Kim, Y. Kim, S. U. Yu, K. S. Kim, D. Y. Noh, J. Chung, Proximity effect induced electronic properties of graphene on Bi_2Te_2Se. *ACS Nano* **9**, 10861–10866 (2015).
15. K. Vaklinova, A. Hoyer, M. Burghard, K. Kern, Current-induced spin polarization in topological insulator–graphene heterostructures. *Nano Lett.* **16**, 2595–2602 (2016).
16. L. Zhang, B.-C. Lin, Y.-F. Wu, H.-C. Wu, T.-W. Huang, C.-R. Chang, X. Ke, M. Kurttepeli, G. V. Tendeloo, J. Xu, D. Yu, Z.-M. Liao, Electronic coupling between graphene and topological insulator induced anomalous magnetotransport properties. *ACS Nano* **11**, 6277–6285 (2017).
17. H. Steinberg, L. A. Orona, V. Fatemi, J. D. Sanchez-Yamagishi, K. Watanabe, T. Taniguchi, P. Jarillo-Herrero, Tunneling in graphene–topological insulator hybrid devices. *Phys. Rev. B* **92**, 241409 (2015).
18. L. Zhang, Y. Yan, H.-C. Wu, D. Yu, Z.-M. Liao, Gate-tunable tunneling resistance in graphene/topological insulator vertical junctions. *ACS Nano* **10**, 3816–3822 (2016).
19. S. Rajput, Y.-Y. Li, M. Weinert, L. Li, Indirect interlayer bonding in graphene–topological insulator van der Waals heterostructure: Giant spin–orbit splitting of the graphene Dirac states. *ACS Nano* **10**, 8450–8456 (2016).
20. M. Rodriguez-Vega, G. Schwiete, J. Sinova, E. Rossi, Giant Edelstein effect in topological-insulator–graphene heterostructures. *Phys. Rev. B* **96**, 235419 (2017).
21. A. Dankert, P. Bhaskar, D. Khokhriakov, I. H. Rodrigues, B. Karpiak, M. V. Kamalakar, S. Charpentier, I. Garate, S. P. Dash, Origin and evolution of surface spin current in topological insulators. *Phys. Rev. B* **97**, 125414 (2018).
22. A. W. Cummings, J. H. Garcia, J. Fabian, S. Roche, Giant spin lifetime anisotropy in graphene induced by proximity effects. *Phys. Rev. Lett.* **119**, 206601 (2017).
23. A. Dankert, S. P. Dash, Electrical gate control of spin current in van der Waals heterostructures at room temperature. *Nat. Commun.* **8**, 16093 (2017).
24. W. Yan, O. Txoperena, R. Llopis, H. Dery, L. E. Hueso, F. Casanova, A two-dimensional spin field-effect switch. *Nat. Commun.* **7**, 13372 (2016).
25. L. A. Benítez, J. F. Sierra, W. S. Torres, A. Arrighi, F. Bonell, M. V. Costache, S. O. Valenzuela, Strongly anisotropic spin relaxation in graphene–transition metal dichalcogenide heterostructures at room temperature. *Nat. Phys.* **14**, 303–308 (2018).
26. T. S. Ghiasi, J. Ingla-Aynés, A. A. Kaverzin, B. J. van Wees, Large proximity-induced spin lifetime anisotropy in transition-metal dichalcogenide/graphene heterostructures. *Nano Lett.* **17**, 7528–7532 (2017).
27. S. Omar, B. J. van Wees, Spin transport in high-mobility graphene on WS_2 substrate with electric-field tunable proximity spin-orbit interaction. *Phys. Rev. B* **97**, 045414 (2018).
28. W. Han, K. Pi, K. M. McCreary, Y. Li, J. J. I. Wong, A. G. Swartz, R. K. Kawakami, Tunneling spin injection into single layer graphene. *Phys. Rev. Lett.* **105**, 167202 (2010).
29. C. L. Kane, E. J. Mele, Z_2 topological order and the quantum spin Hall effect. *Phys. Rev. Lett.* **95**, 146802 (2005).
30. Z. Lin, W. Qin, J. Zeng, W. Chen, P. Cui, J.-H. Cho, Z. Qiao, Z. Zhang, Competing gap opening mechanisms of monolayer graphene and graphene nanoribbons on strong topological insulators. *Nano Lett.* **17**, 4013–4018 (2017).
31. M. Gurram, S. Omar, B. J. Van Wees, Electrical spin injection, transport, and detection in graphene-hexagonal boron nitride van der Waals heterostructures: Progress and perspectives. *2D Mater.* **5**, 032004 (2018).
32. J. Fabian, A. Matos-Abiague, C. Ertler, P. Stano, I. Žutić, Semiconductor spintronics. *Acta Phys. Slov.* **57**, 565–907 (2007).
33. P. Zhang, M. Wu, Electron spin relaxation in graphene with random Rashba field: Comparison of the D'yakonov–Perel' and Elliott–Yafet-like mechanisms. *New J. Phys.* **14**, 033015 (2012).
34. D. Huertas-Hernando, F. Guinea, A. Brataas, Spin-orbit-mediated spin relaxation in graphene. *Phys. Rev. Lett.* **103**, 146801 (2009).
35. H. Ochoa, A. C. Neto, F. Guinea, Elliot-Yafet mechanism in graphene. *Phys. Rev. Lett.* **108**, 206808 (2012).
36. W. Amamou, G. Stecklein, S. J. Koester, P. A. Crowell, R. K. Kawakami, Spin absorption by in situ deposited nanoscale magnets on graphene spin valves. http://arxiv.org/abs/1804.02103 (2018).
37. D. Kochan, M. Gmitra, J. Fabian, Spin relaxation mechanism in graphene: Resonant scattering by magnetic impurities. *Phys. Rev. Lett.* **112**, 116602 (2014).
38. H. Idzuchi, A. Fert, Y. Otani, Revisiting the measurement of the spin relaxation time in graphene-based devices. *Phys. Rev. B* **91**, 241407 (2015).
39. D. Soriano, D. Van Tuan, S. M. Dubois, M. Gmitra, A. W. Cummings, D. Kochan, F. Ortmann, J.-C. Charlier, J. Fabian, S. Roche, Spin transport in hydrogenated graphene. *2D Mater.* **2**, 022002 (2015).
40. L. Kou, B. Yan, F. Hu, S.-C. Wu, T. O. Wehling, C. Felser, C. Chen, T. Frauenheim, Graphene-based topological insulator with an intrinsic bulk band gap above room temperature. *Nano Lett.* **13**, 6251–6255 (2013).
41. C. L. Kane, E. J. Mele, Quantum spin Hall effect in graphene. *Phys. Rev. Lett.* **95**, 226801 (2005).
42. M. Gmitra, D. Kochan, P. Högl, J. Fabian, Trivial and inverted Dirac bands and the emergence of quantum spin Hall states in graphene on transition-metal dichalcogenides. *Phys. Rev. B* **93**, 155104 (2016).
43. J. Wang, S.-C. Zhang, Topological states of condensed matter. *Nat. Mater.* **16**, 1062–1067 (2017).
44. W. Kohn, L. J. Sham, Self-consistent equations including exchange and correlation effects. *Phys. Rev.* **140**, A1133–A1138 (1965).
45. G. Kresse, J. Furthmüller, Efficiency of ab-initio total energy calculations for metals and semiconductors using a plane-wave basis set. *Comput. Mater. Sci.* **6**, 15–50 (1996).
46. G. Kresse, D. Joubert, From ultrasoft pseudopotentials to the projector augmented-wave method. *Phys. Rev. B* **59**, 1758–1775 (1999).
47. J. P. Perdew, K. Burke, M. Ernzerhof, Generalized gradient approximation made simple. *Phys. Rev. Lett.* **77**, 3865–3868 (1996).
48. A. Tkatchenko, M. Scheffler, Accurate molecular van der Waals interactions from ground-state electron density and free-atom reference data. *Phys. Rev. Lett.* **102**, 073005 (2009).

49. S. Hikami, A. I. Larkin, Y. Nagaoka, Spin-orbit interaction and magnetoresistance in the two dimensional random system. *Progr. Theor. Exp. Phys.* **63**, 707–710 (1980).
50. D. Takane, S. Souma, T. Sato, T. Takahashi, K. Segawa, Y. Ando, Work function of bulk-insulating topological insulator $Bi_{2-x}Sb_xTe_{3-y}Se_y$. *Appl. Phys. Lett.* **109**, 091601 (2016).
51. Y.-J. Yu, Y. Zhao, S. Ryu, L. E. Brus, K. S. Kim, P. Kim, Tuning the graphene work function by electric field effect. *Nano Lett.* **9**, 3430–3434 (2009).
52. D. K. Schroder, *Semiconductor Material and Device Characterization* (John Wiley & Sons, 2006).

Acknowledgments: We thank our colleagues at the Quantum Device Physics Laboratory and Nanofabrication Laboratory at Chalmers University of Technology for support. **Funding:** Chalmers researchers acknowledge financial support from the European Union (EU) Horizon 2020 Research and Innovation Programme GrapheneCore2 contract number 785219 (Graphene Flagship), EU FLAG-ERA project (from Swedish Research Council VR no. 2015-06813), Swedish Research Council VR project grants (no. 2016-03658), Graphene Center, and the AoA Nano program at Chalmers University of Technology. Catalan Institute of Nanoscience and Nanotechnology (ICN2) was supported by the Severo Ochoa program from Spanish Ministry of Economy and Competitiveness (MINECO; grant no. SEV-2013-0295) and funded by the Centres de Recerca de Catalunya Programme/Generalitat de Cataluña. S.R. acknowledges the Spanish MINECO and the European Regional Development Fund (project no. FIS2015-67767-P MINECO/FEDER), and the Secretaría de Universidades e Investigación del Departamento de Economía y Conocimiento de la Generalitat de Cataluña (2014 SGR 58).
Author contributions: D.K. and S.P.D. conceived and planned the experiments. A.W.C. and S.R. conceived the theoretical calculation ideas. D.K. fabricated the devices and performed measurements with support from A.D. and B.K. A.W.C. and M.V. analyzed and interpreted the theoretical data. K.S. provided the calculated data. D.K., A.D., and S.P.D. analyzed the experimental data. D.K., A.W.C., S.R., and S.P.D. compiled the figures and wrote the manuscript. All authors discussed the results and provided feedback on the manuscript. S.P.D. and S.R. supervised the experimental and theoretical research, respectively. **Competing interests:** The authors declare that they have no competing interests. **Data and materials availability:** All data needed to evaluate the conclusions in the paper are present in the paper and/or the Supplementary Materials. Additional data related to this paper may be requested from the authors.

Submitted 19 April 2018
Accepted 9 August 2018
Published 21 September 2018
10.1126/sciadv.aat9349

Citation: D. Khokhriakov, A. W. Cummings, K. Song, M. Vila, B. Karpiak, A. Dankert, S. Roche, S. P. Dash, Tailoring emergent spin phenomena in Dirac material heterostructures. *Sci. Adv.* **4**, eaat9349 (2018).

Tailoring emergent spin phenomena in Dirac material heterostructures

Dmitrii Khokhriakov, Aron W. Cummings, Kenan Song, Marc Vila, Bogdan Karpiak, André Dankert, Stephan Roche and Saroj P. Dash

Sci Adv **4** (9), eaat9349.
DOI: 10.1126/sciadv.aat9349